

An Anatomically Detailed Arterial Network Model for One-Dimensional Computational Hemodynamics

Pablo J. Blanco*, Sansuke M. Watanabe, Marco Aurélio R. F. Passos, Pedro A. Lemos, and Raúl A. Feijóo

Abstract—Simulation platforms are increasingly becoming complementary tools for cutting-edge cardiovascular research. The interplay among structural properties of the arterial wall, morphometry, anatomy, wave propagation phenomena, and ultimately, cardiovascular diseases continues to be poorly understood. Accurate models are powerful tools to shed light on these open problems. We developed an anatomically detailed computational model of the arterial vasculature to conduct 1-D blood flow simulations to serve as simulation infrastructure to aid cardiovascular research. An average arterial vasculature of a man was outlined in 3-D space to serve as geometrical substrate for the mathematical model. The architecture of this model comprises almost every arterial vessel acknowledged in the medical/anatomical literature, with a resolution down to the luminal area of perforator arteries. Over 2000 arterial vessels compose the model. Anatomical, physiological, and mechanical considerations were employed for the set up of model parameters and to determine criteria for blood flow distribution. Computational fluid dynamics was used to simulate blood flow and wave propagation phenomena in such arterial network. A sensitivity analysis was developed to unveil the contributions of model parameters to the conformation of the pressure waveforms. In addition, parameters were modified to target model to a patient-specific scenario. On the light of the knowledge domain, we conclude that the present model features excellent descriptive and predictive capabilities in both patient-generic and patient-specific cases, presenting a new step toward integrating an unprecedented anatomical description, morphometric, and simulations data to

help in understanding complex arterial blood flow phenomena and related cardiovascular diseases.

Index Terms—Blood flow, 1-D model, patient specific, vascular anatomy, waveforms.

I. INTRODUCTION

SINCE the 1950s, there have been increasing efforts to develop computational models and simulation-based techniques to assess physiological and pathophysiological conditions accounting for the multiple time scales and levels of spatial organization present in the cardiovascular system (CVS). Applications such as diagnosis, treatment and surgical planning have been enormously benefitted from these complementary tools [1]–[12].

It has also been recognized in the scientific community that an integrative approach to the modeling of the CVS would have to be able to model and simulate the mutual interactions between phenomena taking place at these different time and spatial scales, going from genes expression to the whole organism functioning [13]. As a consequence, it would be possible to have at hand more adequate patient-specific diagnoses and patient-generic treatment of cardiovascular diseases [14].

With the rapid growth in computational resources, models have evolved in sophistication from compartmental to distributed models. Although the study of several cardiovascular diseases requires fully detailed description of the blood flow, to date, 1-D modeling constitutes the preferred approach to simulate systemic interactions, which determine pressure and flow rate waveforms, providing an accurate description of the behavior of the CVS at a reasonable cost.

From pioneer works studying the basic theoretical ingredients [15]–[19], going through the early developments of topological descriptions of the CVS [20]–[25], subsequent improvements and alternatives [26]–[30], and finally, reaching incontestable *in vitro* validations and *in vivo* verifications [31]–[35], as well as *in silico* comparisons against 3-D models [36], 1-D models of the arterial blood flow have had a prolific existence. In fact, the 1-D model is starting to be used as baseline model to test data assimilation techniques for parameter estimation [37]. Should this combination is proved successful, it can be a powerful tool for the development of accurate patient-specific models for surgical procedures (see, for instance, [9], [10] and [38]).

Specifically, the features of a 1-D model can be classified in terms of several attributes (see [34, Table 1]). This classification can be split into two main branches: 1) modeling ingredients, such as arterial wall behavior, shear stress formulation, treatment of the convective acceleration, outflow conditions and 2) topological features, which basically consists of the degree of

Manuscript received May 19, 2014; revised August 31, 2014 and October 15, 2014; accepted October 16, 2014. Date of publication October 22, 2014; date of current version January 16, 2015. This work was supported in parts by the Brazilian agencies CNPq and FAPERJ. Asterisk indicates corresponding author.

*P. J. Blanco is with the Computer Science Department, National Laboratory for Scientific Computing, Ministry of Science, Technology and Innovation, Av. Getúlio Vargas 333, Petrópolis 25651-075, Brazil, and also with the National Institute of Science and Technology in Medicine Assisted by Scientific Computing, Brazil (e-mail: pjblando@lncc.br).

R. A. Feijóo is with the Computer Science Department, National Laboratory for Scientific Computing, Ministry of Science, Technology and Innovation, Av. Getúlio Vargas 333, Petrópolis 25651-075, Brazil, and also with the National Institute of Science and Technology in Medicine Assisted by Scientific Computing, Brazil (e-mail: feij@lncc.br).

S. M. Watanabe is with the Federal Rural University of Pernambuco UFRPE, Av. Bom Pastor, s/n, Boa Vista, Garanhuns-PE 55292-270, Brazil and also with the National Institute of Science and Technology in Medicine Assisted by Scientific Computing, Brazil (e-mail: sansuke@uag.ufrpe.br).

M. A. R. F. Passos is with the Department of Anatomy, State University of Rio de Janeiro, UERJ, R. São Francisco Xavier 524, Rio de Janeiro 20550-900, Brazil, with the Department of Anatomy, Medical School of Petrópolis, Av. Barão do Rio Branco 905, Petrópolis 25680-120, Brazil and also with the National Institute of Science and Technology in Medicine Assisted by Scientific Computing, Brazil (e-mail: passos@uerj.br).

P. A. Lemos is with the Heart Institute, University of São Paulo Medical School, INCOR-FM-USP, Av. Dr. Eneas de Carvalho Aguiar 44, São Paulo 05403-000, Brazil and also with the National Institute of Science and Technology in Medicine Assisted by Scientific Computing, Brazil (e-mail: pedro.lemos@incor.usp.br).

This paper has supplementary downloadable material available at <http://ieeexplore.ieee.org> (File size: 24 MB).

Digital Object Identifier 10.1109/TBME.2014.2364522

completeness in the description of the arterial vessel connectivity in the model. Anticipating what is to come in the next paragraphs, this paper contributes to the latter point.

A combination of the branching structure of the CVS and of the blood flow distribution to organs is responsible for the reflections pattern. This complex architectural assembly of compliant tapered pipes, combined with dissipation effects, yields a pressure pulse with marked differences when moving distally, from central to peripheral arteries. The reason to develop a detailed description of the cardiovascular network lies on multiple and diversified motivations. Compulsorily, when a more accurate analysis of the systemic interactions is sought, a higher definition in the vascular anatomy that defines blood flow circulation is required.

Defining a model of the CVS implies truncating the arterial network at a certain level. This truncation introduces natural limitations to the model with respect to predicting hemodynamic quantities (pressure and flow) at specified locations in the network. With a large number of arterial vessels in the definition of the vascular anatomy, it is possible to carry out investigations on both central and regional hemodynamics and their interplay, as well as to establish the fundamental connection between the arterial architecture and the differential (and regionally distributed) blood supply within organs and other vascular territories through perforator vessels. This sole fact constitutes a monolithic argumentation for the development of a highly detailed topological description of the vascular anatomy in the CVS.

The aim of this study is to make use of available anatomical data and physiological concepts to create an unprecedented and groundbreaking computational model of the entire arterial network to set the groundwork to perform cutting-edge cardiovascular research supported by modeling of physical phenomena and simulation-based techniques. Hereafter, we use the appellation ADAN model that stands for *Anatomically Detailed Arterial Network model*. In the arterial topology of the ADAN model, segments, branching points, anastomoses, and collateral circuits are mapped into an anatomically realistic 3-D space in compliance with the field of knowledge of descriptive anatomy. Also, the concept of perforator arteries and vascular territories is merged with modeling entities to aid in the definition of blood flow distribution. This results in a truly realistic and anatomically consistent arterial organization that enables setting up, from the hemodynamics point of view, a wide range of physiological and pathophysiological cardiovascular scenarios. A discussion of the role of this kind of model in clinical and modeling applications is given in the Section IX of the Supplementary Material.

With respect to the underlying mathematical model, we do not go into unnecessary sophistication, which may obscure the novelty of this study. We make use of well-established 1-D Navier–Stokes equations in compliant vessels and lumped Windkessel models for the peripheral beds. Specifically, a nonlinear viscoelastic wall behavior is used with nonlinearities arising from collagen contribution. Also, tapering in arterial vessels is considered.

Criteria for the selection and determination of geometrical parameters are exposed, as well as the criteria for the setting of material parameters and outflow conditions. Finally, numerical results are presented, and the global features of the blood circulation predicted by the ADAN model are discussed. These results prove that the so-constructed model produces physiologically meaningful results, which are in agreement with published patient records at different levels of comparison.

The model is further assessed through a detailed sensitivity analysis in which regional perturbations of model parameters are carried out to evaluate the impact on the pressure pulse in central and peripheral arteries. At last but not least, some of the model parameters are modified to target pressure measurements taken from a specific young subject. Such comparisons against *in vivo* data from the same subject provide clear evidence of the predictive capabilities of the ADAN model.

This paper is organized as follows. In Section II, the arterial network is described. In Section III, the criteria to define model parameters is exposed. Governing equations and complementary model parameters are presented in the Sections I–IV of the Supplementary Material. Numerical assessment of the hemodynamics in a healthy subject is presented in Section IV. The sensitivity analysis is developed in Section V, while comparisons against patient-specific pressure measurements are performed in Section VI. Finally, concluding remarks are outlined in Section IX.

II. GLOBAL FEATURES OF THE ADAN MODEL

The ADAN model was outlined in 3-D space using data extracted from classical anatomical textbooks [39], [40], featuring the average vascular anatomy of a man. Arterial pathways were mapped aided by a digital dataset of a human skeleton as scaffold. Almost every single arterial vessel with a well-established name according to the anatomical terminology has been included in the model. The convention employed here follows [39], which is the International Anatomical Terminology. This amounts to have, within the model, 1598 named arteries, plus 544 smaller vessels called perforator arteries, which ultimately supply blood to peripheral regions. Overall, 2142 arterial vessels are in the model, considering repetitions. Arterial segments were drawn using cubic splines in software Autodesk 3ds Max (version 2010).

The model is 170 cm in height, with an equivalent body surface area 16488 cm² (measured from the surface of vascular territories, see [41]). With respect to morphometry, vessel lengths resulted naturally from combining branching/anastomotic locations, retrieved from the descriptive anatomy textbooks, and taking into account the measures of the scaffold. In turn, the diameter of each arterial vessel was retrieved from studies published in the literature, and processed as explained in Section III. This resulted in a large dataset, which represents a unique data collection complementing descriptive anatomy textbooks. The number of specific organs (kidneys, liver, etc.) to which blood is supplied is 28 and the number of vascular territories considered

to split blood delivery to distributed organs (muscles, skin, etc.) is 116. The full model dataset has been made publicly available at <http://hemolab.lncc.br/adan-web> (see [42]).

Fig. 1, Panel (a), displays the ADAN model on top of the human skeleton, for ease of visualization. Observe that the large collateral circulations are present in the model. For instance, the redundant circulation in the neck and head and the extracranial vasculature, as well as the complex vascularization of the brain (Panel (b)); the posterior intercostal arteries arising from the aorta to join the anterior intercostal arteries, which arise from the internal thoracic artery (Panel (c)); the mesenteric circuits including the anastomotic arcades of ileal and jejunal arteries (Panels (d) and (f)). Other instances include the patellar network of the knee; and palmar and plantar arches, among others. In Fig. 1, Panels (e) and (f), respectively, present a direct comparison of the vascular structures of kidneys and mesentery against real anatomic pieces prepared in the Anatomy Department of the Medical School of Petrópolis. Such comparison makes evident that the complexity of the real vascular anatomy is accounted for in the ADAN model.

It is worthwhile to highlight that the line drawing in 3-D space was motivated by

- 1) the resulting undeniable visual appealing of the ADAN model for the medical community;
- 2) the straightforward possibility of using the ADAN model as an anatomical and functional atlas [42];
- 3) the development of enriched 1-D blood flow models to account for curvature effects on hemodynamics [43], [44].

III. GEOMETRICAL PARAMETERS

A. Vessel Length

Vessel lengths resulted from drawing in 3-D the arterial vessels on top of the digital skeleton employed as scaffold (see [42]). Most of the arterial vessels have multiple occurrences. In such cases, the lengths may vary, and the range reported there stands for such occurrence variability.

B. Lumen Radius

1) *Data Sweeping*: Raw data were obtained from morphometric, anatomic, clinical, and surgical studies, among others. This comprised two kinds of data: external diameters from dissection studies, and lumen radii from imaging studies. After this data sweeping process, the bibliographic data were organized according to the main regions of the body. The comprehensive list of final papers from which data were retrieved is provided in [42].

2) *Data Selection*: From the raw data, the final value of vessel diameter was defined considering the following criteria.

- 1) *Range*: Most of publications in the field report average and standard deviation or min–max range for arterial diameters; in any case, the final arterial diameter is always within the ranges reported in the literature.
- 2) *Gender*: When specified, data for males were selected.

- 3) *Hierarchy*: Criteria were first applied to define the diameter of larger arteries, and just after this, the diameter of smaller vessels was defined.
- 4) *Coherence*¹: Vessel diameter always respected proximal–distal coherence, that is, a given vessel is always larger than branching vessels located downstream.
- 5) *Source Data*: A given radius was defined based either on dissection studies or on imaging studies, in any case, were these two sources of data combined.
- 6) *Type*: As with the source data, a certain radius was defined based either on internal diameter data or on external diameter data.
- 7) *Exceptions*: In the case of lack of data, arterial diameter was estimated using four different approaches.
 - a) *Murray law*: The relation between the radius of the upstream vessel R_u and downstream vessels R_{d1}, R_{d2} follows the power law (Murray law): $R_u^3 = R_{d1}^3 + R_{d2}^3$.
 - b) *Neighborhood*: The radius is considered to be equal to surrounding vessels (for instance, the anterior superior pancreaticoduodenal artery is located as the continuation of the gastroduodenal artery and preceding the inferior pancreaticoduodenal artery, so the average of the last two arteries was used for the former one).
 - c) *Similarity*: The vessel radius is equal to the radius of an anatomically similar vessel (for instance, posterior tympanic artery was considered similar to the superior tympanic artery).
 - d) *Image measure*: The vessel radius is estimated from the relative measure between an unknown arterial radius and some known surrounding vessel radius (for instance, the umbilical artery was estimated by comparing it to the internal iliac artery).

Noteworthy, just 101 out of 1598 arterial vessels (6.3%) in the model were exceptions.

3) *Determination of Lumen Radii*: In some cases, the definition of arterial caliber was based on imaging studies from which internal diameters were retrieved, say D_i . However, most of the times, the arterial diameter was defined based on dissection studies reporting the external vessel diameter, say D_e . Then, the internal radius R was finally obtained as follows:

$$\begin{cases} 2R_o = D_i & \text{imaging studies} \\ 2R_o \left(1 + \frac{h}{R_o}\right) = D_e & \text{dissection studies.} \end{cases} \quad (1)$$

The second formula relies on the known value of the arterial wall thickness h , or equivalently on the known relation h/R_o , which in this study is related to the internal radius (see next section).

¹The notion of upstream–downstream direction is lost when anastomoses are present. Here, it is important to recall that anastomoses are usually formed by small collateral vessels that connect larger arteries (for instance, the intercostal arteries connecting the internal thoracic artery to the thoracic aorta. Hence, at each extreme of these collateral vessels, upstream direction is dictated by the proximal direction of the main vessel the collateral is attached to. In this manner, collaterals satisfy coherence by being considered downstream vessels with respect to the main vessels they branch off -at both extreme points-.

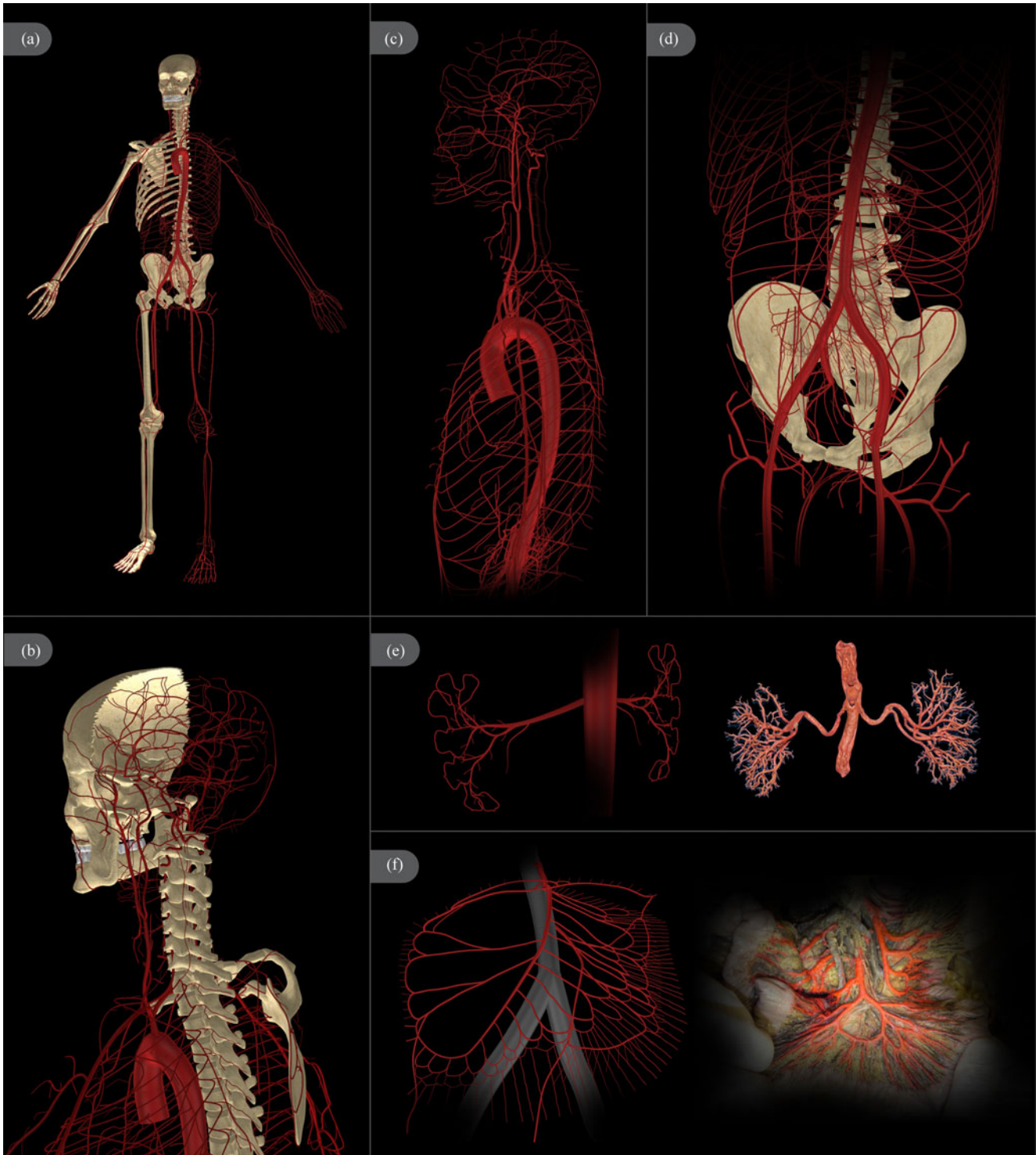


Fig. 1. Unique vascular anatomy of the ADAN model comprising: 1598 named arteries, 544 perforator vessels, blood supply to 28 specific organs, and to 116 vascular territories.

4) *Arterial Tapering*: Linear tapering was considered for the larger vessels. In all cases, the definition of the tapering was such that proximal–distal coherence was satisfied (see Section III-B2).

C. Wall Thickness

In [26], the lumen radius R_o and wall thickness h are reported for a large number of arterial vessels. Curve fitting of such data

was performed to produce the following relation:

$$\frac{h}{R_o} = ae^{(bR_o)} + ce^{(dR_o)} \quad (2)$$

with $a = 0.2802$, $b = -5.053$ 1/cm, $c = 0.1324$ and $d = -0.1114$ 1/cm.

IV. HEMODYNAMICS IN THE ADAN MODEL

In this section, numerical simulations are presented. Standard governing equations for the flow of an incompressible fluid in compliant pipes are considered in each arterial segment. Proper coupling conditions at junctions are also postulated, as well as terminal Windkessel models. The full set of equations is given in Section I of the Supplementary Material. Model parameters related to arterial wall behavior and terminal models are calibrated using criteria exposed in Sections II and III of the Supplementary Material, respectively. The interested reader is referred to [41] for a detailed account on the criteria to distribute flow to organs and other vascular territories. Additional ingredients present in the numerical simulations can also be found in the Supplementary Material.

First, we present and discuss pressure and flow waveforms. Second, some well-known cardiovascular indexes are introduced to assess the overall cardiovascular state predicted by the model, also performing a comparison with reference values. A word on validation/verification is given at the end of the section.

A mechanistic discussion of the model predictions and of the sensitivity analysis (see Section V), using for example, wave intensity analysis [45] and decomposition of waveforms into forward and backward travelling waves [46], is out of the scope of this paper and will be a matter of a future contribution.

A. Pressure and Flow Rate Waveforms

The panels presented in Fig. 2 display the pressure (solid line) and blood flow rate (dashed line) contours obtained with the ADAN model at several arterial vessels (additional results are reported in the Supplementary Material). The waveforms predicted by the ADAN model through the aorta artery (Panels 8–11) follow closely results encountered in the specialized literature.

The pressure pulse at the aortic root (Panel 8) is a typical record, which corresponds to a healthy young subject [47], with the characteristic concave diastolic decay [48]. At the thoracic aorta (Panel 9), a characteristic flow waveform is predicted, in agreement with [34]. Blood flow in the abdominal aorta (supraceliac location, Panel 10) features a biphasic waveform with flow reversal in early diastole, while a triphasic waveform with forward flow in late diastole is observed in the distal part of the abdominal aorta (infrarenal location, Panel 11), which is in agreement with measurements in normal subjects [49].

Arterial segments supplying abdominal organs (Panels 12–17) present characteristic waveforms, which are well predicted by the present model according to measurements in control patients, in particular flow at the superior and inferior mesenteric arteries (Panels 12 and 13, respectively) as well as liver vessels

(common hepatic and proper hepatic arteries, Panels 14 and 15, respectively) [50], [51]. Specifically, low resistance flow signatures (unidirectional flow) are observed at arteries supplying vascular beds, which require continuous blood supply such as hepatic vessels and renal arteries (Panel 16), while high resistance patterns (alternating flow direction and reduced diastolic flow) are observed in vascular beds such as those supplied by the mesenteric arteries (at fasting state) and the gastric vessels (Panels 17). The main complex of vessels supplying the lower limb (common iliac-external iliac-femoral-popliteal-posterior tibial, Panels 18–22) features a triphasic flow contour which is a classical signature of the blood flow at those locations. The pressure pulse predicted at the posterior tibial artery (Panel 22) is very close to measurements published in [52].

With regard to the vessels supplying the brain, at the common carotid artery (Panel 1), the flow is in close agreement with experimental findings in [53], featuring a mixed type of flow curve, which is the result of a low resistance signature from the internal carotid (Panel 2), indicating continuous flow supply as required by the brain, and a high resistance signature from the external carotid (Panels 3), resulting in minimal diastolic flow directed toward the extracranial region [51]. In the same manner, flow at the vertebral and basilar arteries (Panels 4 and 5, respectively), as well as other arteries in the brain such as the anterior cerebral artery and the pericallosal artery (Panels 7 and 6, respectively) present antegrade flow supply. A quantitative analysis of regional brain flow distribution in the ADAN model matches ranges reported in [54] concerning the tributary arteries to the circle of Willis, as shown in Table I. We highlight that the data in Table I taken from [54] were not used in the calibration process.

Alteration of the pressure pulse as it travels along the aorta toward the lower limbs is in good agreement with results published in [33] (see also Fig. 3). The dicrotic notch in the pressure pulse smoothes out as we move distally, while the anacrotic pulse becomes steeper as we move from central to distal locations. In turn, mean, systolic, and diastolic pressures are within the values found in healthy population. This can be seen in Fig. 3, where the pressure pulse is shown as we move from the aortic root to the peripheral regions, particularly toward the lower limb. While the mean pressure decrease is of the order of 4 mmHg, diastolic pressure reduces 10 mmHg, and systolic pressure increases 30 mmHg. In such figure, it is evident the wave propagation phenomenon and the increase in the steepness of the anacrotic pulse. This pressure propagation phenomenon can be better appreciated through the animated visualization available as Supplementary Material.

B. Input Impedance

Impedance analysis has been widely used for characterizing the arterial system (see [47] and [55] and references therein). Main reflection patterns are manifested in the aortic impedance, and the oscillatory behavior is able to indicate some global features of the arterial function, such as impedance mismatch. The impedance Z -modulus and phase- at the aortic root was

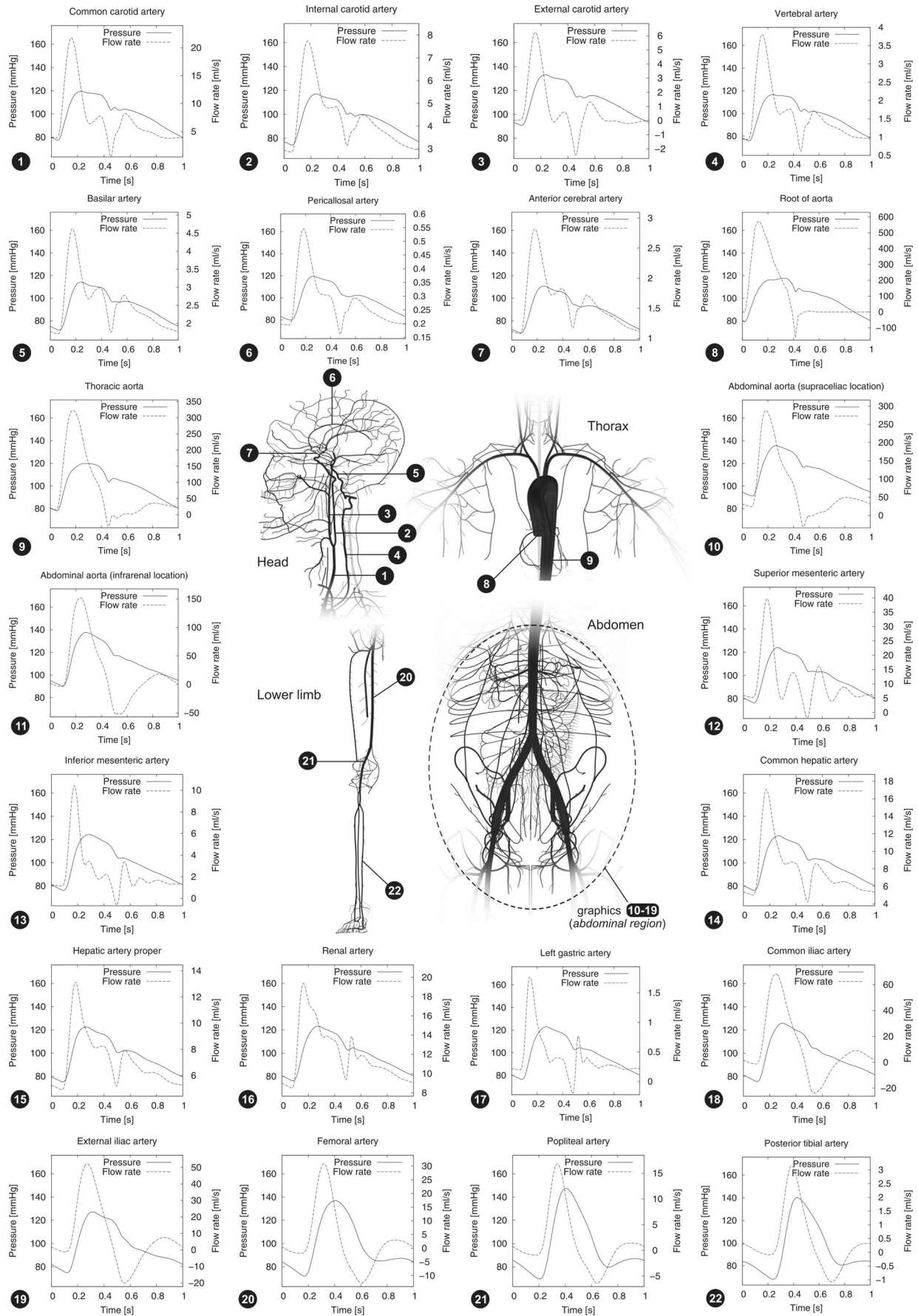


Fig. 2. Pressure (solid) and flow rate (dashed) in the main arterial segments.

TABLE I
AVERAGE FLOW RATES IN THE TRIBUTARIES OF THE CIRCLE OF WILLIS

Artery	Avg. flow rate Q [ml/min]	
	ADAN model	Ref. values ¹
CCA	429	389 (73)
VA	90	96 (38)
ICA	257	264 (52)
MCA	125	150 (31)
ACA	70	85 (26)
PCA	65	66 (14)
PcomA	3*	17 (25)
BA	151	131 (40)

¹: [54] on left side, mean (std. dev.). CCA: common carotid artery, VA: vertebral artery, ICA: internal carotid artery, MCA: middle cerebral artery, ACA: anterior cerebral artery, PCA: posterior cerebral artery, PcomA: posterior communicating artery, BA: basilar artery. *: direction of blood flow is from PCA to ICA.

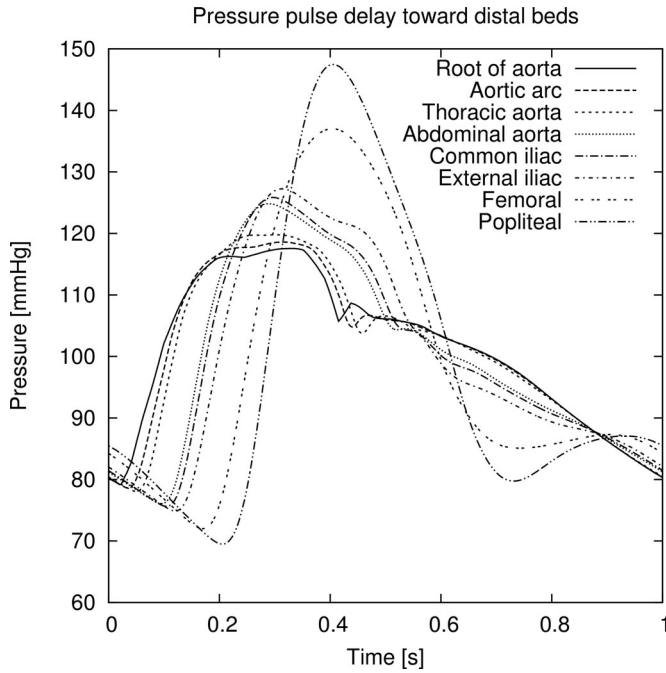


Fig. 3. Pressure waveforms in arterial vessels as a function of their distance to the aortic root.

computed as a function of the frequency f . Fig. 4 presents the results up to the 14th harmonic.

Impedance at zero frequency is $Z_0 = 1205 \text{ dyn s/cm}^5$, while characteristic impedance, taken as the average of the impedance moduli for frequencies larger than 2 Hz, is $Z_C = 46 \text{ dyn s/cm}^5$. These values are very close to the data reported in [47] ($Z_0 = 1168 \pm 80 \text{ dyn s/cm}^5$ and $Z_C = 45 \pm 7 \text{ dyn s/cm}^5$). Fig. 4 shows the relative value of the impedance to the characteristic impedance (Z/Z_C) and the impedance phase. In general, the model features an impedance spectrum in compliance with a type B curve according to [47]. According to the data reported in that work, type B curve corresponds, in average, to a 33-year-old subject.

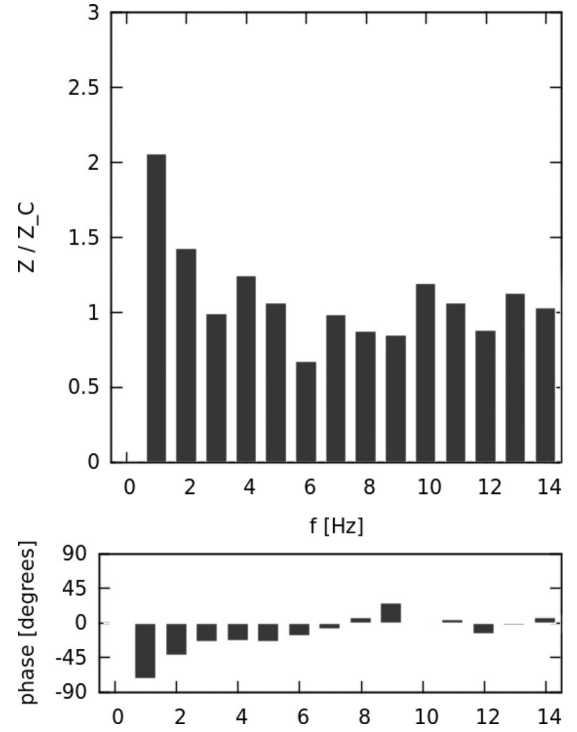


Fig. 4. Input impedance spectrum expressed in modulus and phase. Modulus is nondimensionalized by the characteristic impedance Z_C .

TABLE II
HEMODYNAMIC VARIABLES AND CARDIOVASCULAR INDEXES AS PREDICTED BY THE ADAN MODEL

Index	ADAN model	Ref. values
HR [bpm]	60	81 ¹
CO [L/min]	6.73	7.01 ¹
(DBP-SBP) [mmHg]	(79–118)	(80–114) ¹
AI _A	3.77	[0, 15] ³
AI _C	−6.93	[−20, 0] ⁴
ABI	1.11	[1.11, 1.40] ²
PPA	1.2	[1.5, 1.9] ⁵
PWV _{AF} [cm/s]	545	[500, 1100] ⁴
PWV _{CF} [cm/s]	505	[550, 1100] ⁶
PWV _{BD} [cm/s]	564	[800, 1400] ⁷
PWV _{FD} [cm/s]	623	[600, 1000] ⁷

Reference values are taken for young healthy subjects (< 30 yr) as follows: ¹: [47], mean of 11 subjects, curves type B and C. ²: [56]. ³: [47], [57]. ⁴: [58]. ⁵: [59]. ⁶: [60]. ⁷: [61]. HR: heart rate, CO: cardiac output, SBP: systolic blood pressure, DBP: diastolic blood pressure, AI: augmentation index, ABI: ankle-brachial index. PPA: pulse pressure amplification. PWV: pulse wave velocity. Subscripts (arteries): A: ascending aorta, B: brachial, C: common carotid, F: femoral, D: dorsalis pedis.

C. Cardiovascular Indexes

In Section VII of the Supplementary Material, the motivation-to-use and definition of several cardiovascular indexes is given. All the values for these indexes predicted by the ADAN model are reported in Table II. In such table, some reference values are given. It is worthwhile to comment that all these indexes are within the ranges corresponding to healthy young subjects. Although these data were taken from diverse reference studies,

TABLE III
PULSATILITY INDEX IN BRAIN ARTERIES

Artery	D_{ao} [cm]	PI	PI ¹
CCA p.	9.5	2.748	
CCA d.	19	2.268	
ICA p.	21.6	1.080	1.20 (0.26)
ICA d.	33.7	0.825	1.13 (0.21)
MCA	34.9	0.869	1.11 (0.22)
MCA ITB	39	0.806	
MCA AGB	44.5	0.694	
MCA PPB	47.9	0.620	
MCA PB	45.3	0.722	
ACA	36.2	0.949	1.05 (0.36)
ACA PFB	39.7	0.612	
PA p.	39.2	1.360	
PA d.	44.2	0.829	
PCA	37.7	0.964	1.00 (0.21)
PCA MOB	40	1.066	
PCA CB	45.6	0.514	
BA p.	34.5	1.183	1.04 (0.25)
BA d.	36.4	0.936	1.00 (0.19)
VA p.	16.1	2.209	
VA d.	31.4	1.212	1.12 (0.20)

D_{ao} : distance to aortic root, PI: pulsatility index, ¹: [62] on left side, mean (std. dev.). CCA: common carotid artery, ICA: internal carotid artery, MCA: middle cerebral artery, ACA: anterior cerebral artery, PA: pericallosal artery, PCA: posterior cerebral artery, BA: basilar artery, VA: vertebral artery, ITB: inferior terminal branch, AGB: angular gyrus branch, PPB: posterior parietal branch, PB: prefrontal branch, PFB: polar frontal branch, MOB: medial occipital branch, CB: calcarine branch, p.: proximal location, d.: distal location.

they provide a glance of the current cardiovascular state of the ADAN model, and the consistency of the calibration criteria.

Table III reports the pulsatility index (PI) for several arteries in the brain. These results are in close agreement with data published in [62], according to which the present model features pulsatility indexes, which are within the range of variability of healthy (nondemented control) subjects. As concluded in [62], this index can be used to assess functionality of brain circulation.

D. On Model Validation/Verification

Regarding validation, previous sections were devoted to comparing our results with multiple data published in the literature, namely: waveforms, arterial impedance, and cardiovascular indexes. We do not claim that model validation/comparison is a closed problem. Instead, we place our work on top of existing validations and verifications of 1-D models, such as those reported in [31], [34], and [35] (see Section VIII, for an extended discussion). We take this for granted, and created the unmatched computational vascular anatomy presented here to perform numerical simulations with a machinery (1-D blood flow solvers), which has already been proved to be reliable. This hypothesis is reasonable because we are not at the level of capillaries, in which suspensions introduce important effects. Yet the behavior of the viscosity can be debatable (see Section VIII), we still rely on the 1-D fluid mechanics governing equations. Indeed, we aimed at showing the ability of the model in predicting physiologically realistic hemodynamic conditions at different sites of the arterial network to simulate physical phenomena, which are far beyond the capabilities of existing computational models of the arterial tree.

TABLE IV
ANATOMICAL REGIONS AND ABBREVIATIONS USED IN THE SENSITIVITY ANALYSIS

Region	SR	Subregion
Trunk	AsAo	Ascending Aorta
	ThAo	Thoracic Aorta
	AbAo	Abdominal Aorta
	In	Intestines
	Pe	Pelvis
Lower Limb	Hi	Hip Thigh
	Kn	Knee
	Le	Lower Leg
	Ft	Foot

SR: subregion name.

V. SENSITIVITY ANALYSIS

In this section, we limit to studying the impact in the pressure waveforms caused by changes in the compliance of vessels (elastic modulus E_e). This parameter is perturbed by a factor θ_e from the baseline situation. Perturbations were defined by setting $\theta_e \in \{1.0, 1.3, 1.6, 2.0, 3.0, 4.0\}$. This choice was motivated by the fact that arterial stiffening is found to be a characteristic present in several cardiovascular diseases (e.g., hypertension and aging). Baseline condition is $\theta_e = 1$. Here, we study the sensitivity with respect to perturbations of parameters on groups of vessels belonging to different vascular regions. In total, the parameter θ_e was canonically perturbed in 23 regions, i.e., $(1, \dots, 1, \theta_e, 1, \dots, 1)$, being different from 1 at region k , $k = 1, \dots, 23$. Here, we limit the presentation to a subset of regions for which perturbation resulted in more expressive sensitivities. This subset of regions is displayed in Table IV (with the corresponding abbreviations).

We stress here that the computed sensitivity is exclusively representative of the arterial network. Evidently, arterial-cardiac coupling is expected to be important when parameters undergo substantial modifications.

The discussion that follows is focused on the sensitivity of the pressure pulse throughout the path defined by the vascular complex formed by the aorta, iliac, femoral, popliteal, tibiofibular, and posterior tibial arteries. We have chosen this path due to the significance when assessing the systemic state by means of different indexes (e.g. ABI, PWV, etc.) involving hemodynamic quantities measured in these arteries.

The sensitivity is quantified in time, through the cardiac cycle, and in space, in terms of the distance to the aortic root, as follows:

$$s_P(t, \xi) = \frac{\tilde{P}_{\theta_e}(t, \xi) - \tilde{P}_1(t, \xi)}{\Delta P_1(t, \xi)} \times 100 \quad t \in [0, T], \xi \in [0, \xi_{\max}] \quad (3)$$

where t is the time coordinate in the cardiac cycle of duration T , ξ defines the distance to the aortic root, with ξ_{\max} the maximum distance given by the distalmost location in the posterior tibial artery, within the calcaneal region, ΔP_1 is the pressure pulse (systolic pressure minus diastolic pressure) in the baseline condition and $\tilde{P}_X(t, \xi)$, $X \in \{1, \theta_e\}$ (baseline: 1 and perturbed θ_e ,

respectively), is the mean-free pressure waveform, hereafter referred to as *normalized pressure*, at position ξ and through time t . The reason to choose a normalized pressure was to reveal the way in which reflections are maximized and/or minimized when altering the regional arterial stiffness.

Sensitivity maps are presented in Fig. 5 (additional sensitivities are reported in the Section VIII of the Supplementary Material). Such maps correspond to the locations for which the maximum absolute value of s_P exceeded 5% for some time instant. In these time-space maps, the first 42 cm characterize the aorta artery, the second 51 cm correspond to the iliac-femoral complex and the last 55 cm are formed by the popliteal-tibiofibular trunk-posterior tibial complex. The horizontal white lines in Fig. 5 demarcate these regions.

Qualitatively, the sensitivity results are similar for the different values of θ_e . Then, we choose to present the sensitivities for the perturbation factor $\theta_e = 4.0$ because it yields more visible changes.

According to (3), increase of the normalized pressure with respect to the baseline condition corresponds to positive values of s_P , while decrease of the normalized pressure is represented by negative values of s_P . In Fig. 5, the white lines indicate the isolines $s_P = 0$.

Alterations in the stiffness of the aortic arch yield a very particular sensitivity map resembling two fingers arising from the aortic root with an inclination given by the pulse wave velocity [see Fig. 5(a)]. The values of s_P are the largest observed in Fig. 5 for the region of the aorta and the region of the iliac-femoral complex (larger finger). Also, the concavity of the pulse at the aortic root is largely determined by the material behavior in the aortic arch (smaller finger). As for the stiffening of the thoracic aorta [see Fig. 5(b)], the s_P map is slightly different from the previous case. Pressure is increased in a wider window of time. However, unlike stiffening the aortic arch, perturbations smooth out as we move to the popliteal-tibiofibular-posterior tibial complex.

Stiffening of the abdominal aorta yields a completely different s_P map [see Fig. 5(c)]. A single finger arises at the aortic root, with smaller sensitivities in the aortic region than previous cases. Right before the iliac bifurcation, the finger is split into two fingers, which travel to the distal beds. This pattern is similar to the one obtained from stiffening the vessels of the pelvis [see Fig. 5(d)]. The first finger from left to right is more affected from the stiffening of the pelvis, while the second finger is similarly affected by stiffening the pelvic vessels or the abdominal aorta.

Stiffening of the region of the hip and thigh [see Fig. 5(e)] feature a s_P map, which is characterized by a single finger in the aortic region arising at the middle part of the cardiac cycle, and two fingers arising right before the iliac bifurcation. Proximally, in the aortic region, the sensitivity s_P is larger when stiffening the region of the hip and thigh than when stiffening the lower leg and the foot (see Supplementary Material), and the same holds for the iliac-femoral complex in the early finger. The s_P map when stiffening the region of the knee [see Fig. 5(f)] is characterized by a single finger in the aortic region arising at the middle part of the cardiac cycle, and two fingers arising right

before the iliac bifurcation. Proximally, in the aortic region, the sensitivity s_P is larger when stiffening the region of the hip and thigh, and the same holds for the iliac-femoral complex in the early finger.

Fig. 6(a) presents the pressure contour for three characteristic locations each one placed in one of the regions analyzed (see regions delimited in Fig. 5). This result is to be used as baseline scenario for comparison against pressure contours displayed in the rest of the plots of Fig. 6.

Note in Fig. 6(b) that the stiffening of the aortic arch has a strong impact in the systolic pressure rise, while making more pronounced the dicrotic notch. It also dominates the definition of the aortic pressure range (systole-to-diastole) not only in the aorta, but also in peripheral vessels. Instead, the stiffening of the thoracic and abdominal aorta affects mostly the mid and late part of the systolic peak, by rounding the systolic peak and vanishing the inflection point, respectively [see Fig. 6(c) and (d)]. Differently from aortic arch stiffening, thoracic and abdominal aorta stiffening do not impact significantly on the amplification of the distal pressure pulse.

From this analysis (see also the Supplementary Material), it can be concluded that the model is able to predict a wide variety of pressure pulses at central and peripheral vessels. The same holds for other peripheral vessels such as vessels supplying the brain and the upper limb. These results are omitted here for the sake of brevity.

This sensitivity analysis has been used to guide the calibration of the ADAN model to target a patient-specific case, as will be seen in Section VI.

VI. CALIBRATION TARGETING A PATIENT-SPECIFIC CASE

This section presents a version of the ADAN model targeted to predict pressure contours obtained from invasive measurements.

A. Patient Description and Data Acquisition

ECG-gated pressure measurements were obtained invasively from a 32 year-old individual with suspected coronary disease. In [63], it is reported that arterial stiffness is increased in patients with premature coronary disease. However, the patient's diagnostic cardiac catheterization revealed no signs of significant coronary obstruction. Measurement of fractional flow reserve of an angiographically intermediate lesion confirmed the absence of coronary stenoses. Pressure measurements were acquired using a fluid-filled cardiac catheter, which run from the femoral artery towards the coronary ostia. In the pathway, pressure contours were acquired at the following locations: ascending aorta, braquiocephalic trunk, left common carotid (proximal), abdominal aorta (renal level), abdominal aorta (above iliac bifurcation), and right external iliac.

From pressure records, ten cardiac cycles were extracted for each arterial vessel. An average pressure waveform was then obtained.

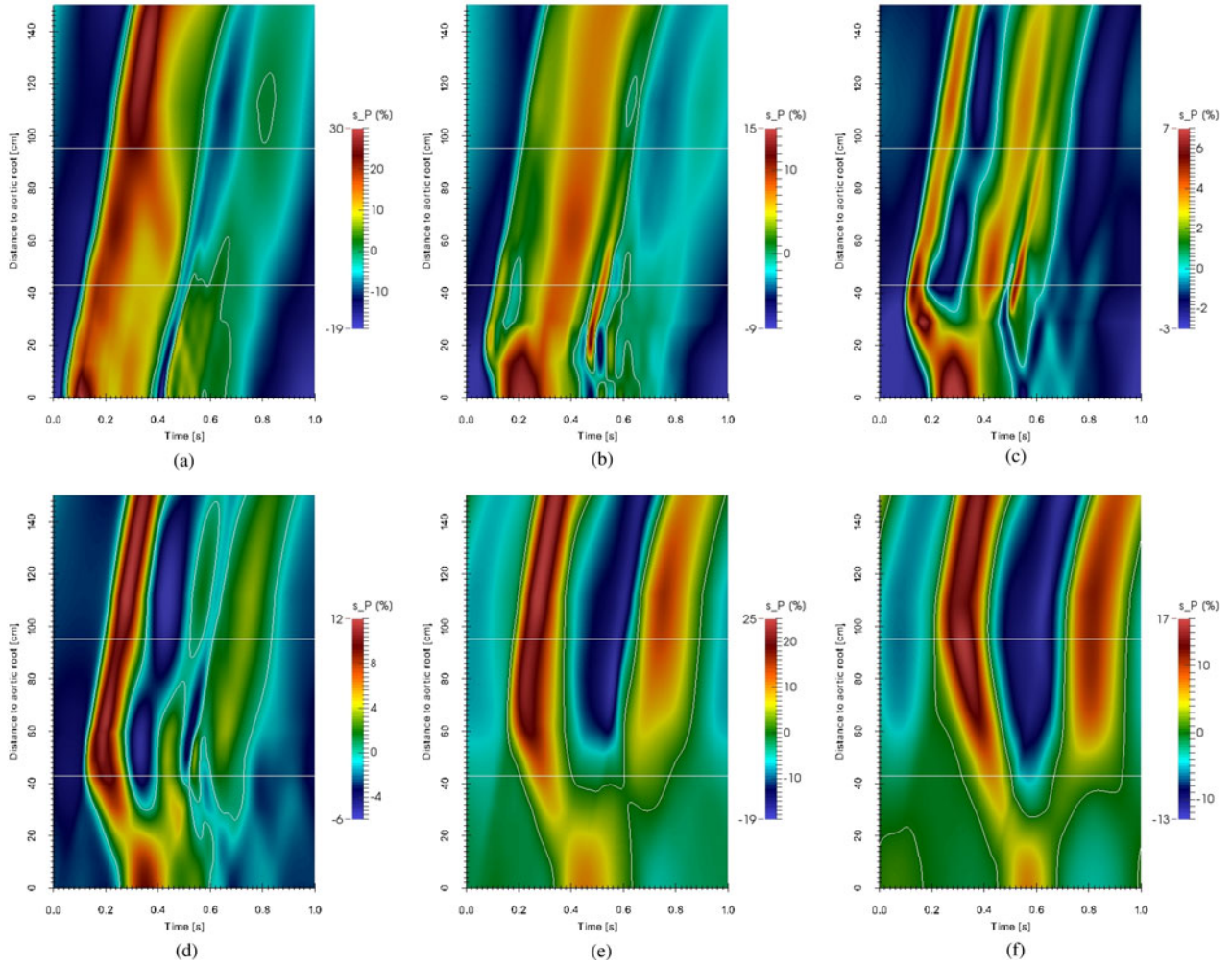


Fig. 5. Sensitivity of the normalized pressure (s_P) throughout the vascular complex aorta-iliac-femoral-popliteal-tibiofibular-posterior tibial arteries for the case $\theta_e = 4.0$. Horizontal lines demarcate the aorta artery, the iliac-femoral and the popliteal-tibiofibular-posterior tibial complexes, respectively. Normalized pressure increase with respect to the baseline condition corresponds to positive values of s_P (toward red), and normalized pressure decrease to negative values of s_P (toward blue). White lines are the $s_P = 0$ isolines (a) Perturbation at AscAo. (b) Perturbation at ThAo. (c) Perturbation at AbAo. (d) Perturbation at Pe. (e) Perturbation at Hi. (f) Perturbation at Kn.

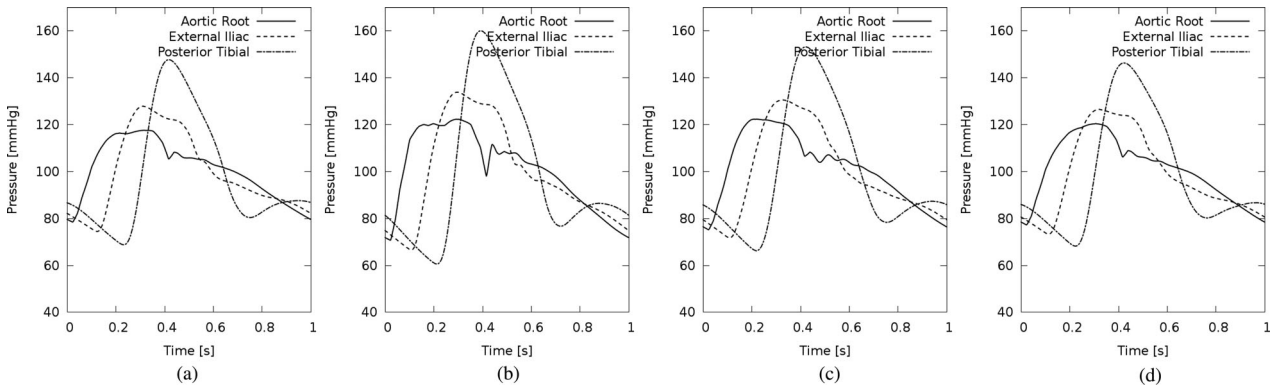


Fig. 6. Pressure contours at three characteristic locations: aorta complex, iliac-femoral complex and popliteal-tibiofibular-posterior tibial complex for the case $\theta_e = 4.0$ (see regions delimited in Fig. 5) (a) Baseline. (b) Perturbation at AscAo. (c) Perturbation at ThAo. (d) Perturbation at AbAo.

B. Model Parameters

The inflow boundary condition was slightly adjusted to match global behavior of the pressure pulse as follows:

- 1) the cardiac period T , which was determined from the ECG, resulting in $T = 0.92$ s;
- 2) the averaged inflow \bar{Q}_{in} was scaled to match normal cardiac output according to age [64], resulting in $\bar{Q}_{in} = 106.76 \text{ cm}^3/\text{s}$ (i.e., 6.4 L/min);
- 3) the inflow upstroke was specified to match the pressure upstroke;
- 4) the time at which flow reversal occurs and the magnitude of backflow were modified to match the position and size of the aortic notch.

Wall model parameters were modified to match the pressure contour predicted by the model with those obtained invasively. By manual inspection, and following the insight obtained with the sensitivity analysis from Section V, the factor θ_e was regionally modified as reported in Table V (denomination of regions follows Table IV). Recall that this parameter modifies the elastic parameter E_e , which for the baseline condition is specified in Section II of the Supplementary Material.

C. Comparison Against Patient-Specific Measurements

The comparison between pressure waveforms is presented in Fig. 7. Overall, the agreement between the results predicted by the ADAN model and the waveforms measured for this specific patient is promising. Remarkably, this affinity has been achieved in a manual manner, guided (by visual inspection) by the sensitivity analysis performed in the previous section. Future developments involving a larger population will require a more objective strategy for assessing and quantifying such agreement.

At the ascending aorta [see Fig. 7(a)], the predicted pressure follows closely the measurement, both during systole and diastole. The overpressure occurring at late systole is diminished and rounded in the ADAN model, being less sharp. The agreement of the waveforms through the abdominal aorta increases as we move distally (see Fig. 7(b) and (c), respectively). The agreement in those cases is better during diastolic decay, while systole is marked by differences in the upstroke and sharpness of the systolic peak. At the external iliac artery [see Fig. 7(d)], the agreement is also satisfactory. The ADAN model predicts a pressure pulse, which is consistent with the measurement in the entire cardiac cycle. As well, the agreement is very good at proximal locations such as the brachiocephalic trunk [see Fig. 7(e)] and the common carotid artery [see Fig. 7(f)]. At these locations, it is observed that both, model and patient, evolve toward a pressure pulse, which, during systole, is more rounded when compared with the pressure contour at the ascending aorta.

The results presented in this section are promising and constitute a small demonstration that the ADAN model is capable of predicting patient-specific conditions, once proper data are available. Even without any information about the inflow condition (just performing basic modifications), it has been possible for the ADAN model to mimic the behavior of the system for this specific patient (in the sense of the available data) with very

TABLE V
FACTOR θ_e AFFECTING THE WALL ELASTIC PARAMETER E_e FROM THE BASELINE CONDITION

Region	AsAo	ThAo	AbAo	Hi	Or	otherwise
θ_e	0.6	1.2	1.6	2.5	1.5	1.0

Or: all abdominal organs.

good agreement in view of all the uncertainties present in the modeling process.

Discrepancies in the pressure waveforms analyzed can be caused by mismatch between the morphometry of the ADAN model and that of the patient, as well as by differences in the spatial location at which data was acquired in the patient and model results were assessed. Also, the measurement of at least one flow rate contour in a central artery would greatly contribute to further improving the predictive capabilities of the ADAN model.

Again, it has to be stressed that the results have been achieved by manual inspection of model parameters (see Table V), and a more objective quantification of the agreement is in order. In this regard, there is room for improving model predictions by pursuing, for instance, a parameter estimation strategy (see [37]).

Evidently, since no further measurements nor data about the patient are available, the obtained parameters may not have a direct relation with the real *in vivo* conditions of the patient. We stress that several basic features of the cardiovascular system were simplified. For instance, it is known that cardiac function can greatly affect pressure pulse formation. This is a limitation of the present model, as discussed in Section VIII.

VII. ANATOMICALLY DETAILED VERSUS 55-ARTERY MODELS

This section presents a qualitative and quantitative analysis of the model predictions by contrast with a model well established in the literature comprising the 55 major arteries. Such simplified model was successfully used in previous publications [29], [65], as well as also as model baseline for the more detailed model developed in [34].

The goal here is to analyze the effect of the highly detailed anatomical vasculature in the model predictions. This analysis is carried out in three cases: 1) the healthy condition, 2) presence of a stenosis in the internal carotid artery (ICA), and 3) presence of stenosis in the subclavian artery (SA).

In all tested cases, time and spatial discretization are the same for both models. The root mean square error (RMSE) is used to perform quantitative comparisons. Pressure RMSE is normalized to the pressure pulse amplitude and the flow rate RMSE is normalized to the maximum systolic flow rate value.

A. Simplified Model Calibration

The 55-artery model was constructed by truncating the ADAN model to the 55 major arteries according to [29]. Hereafter, this model is referred to as “ADAN-55.” Calibration of arterial wall parameters in the ADAN-55 model was performed

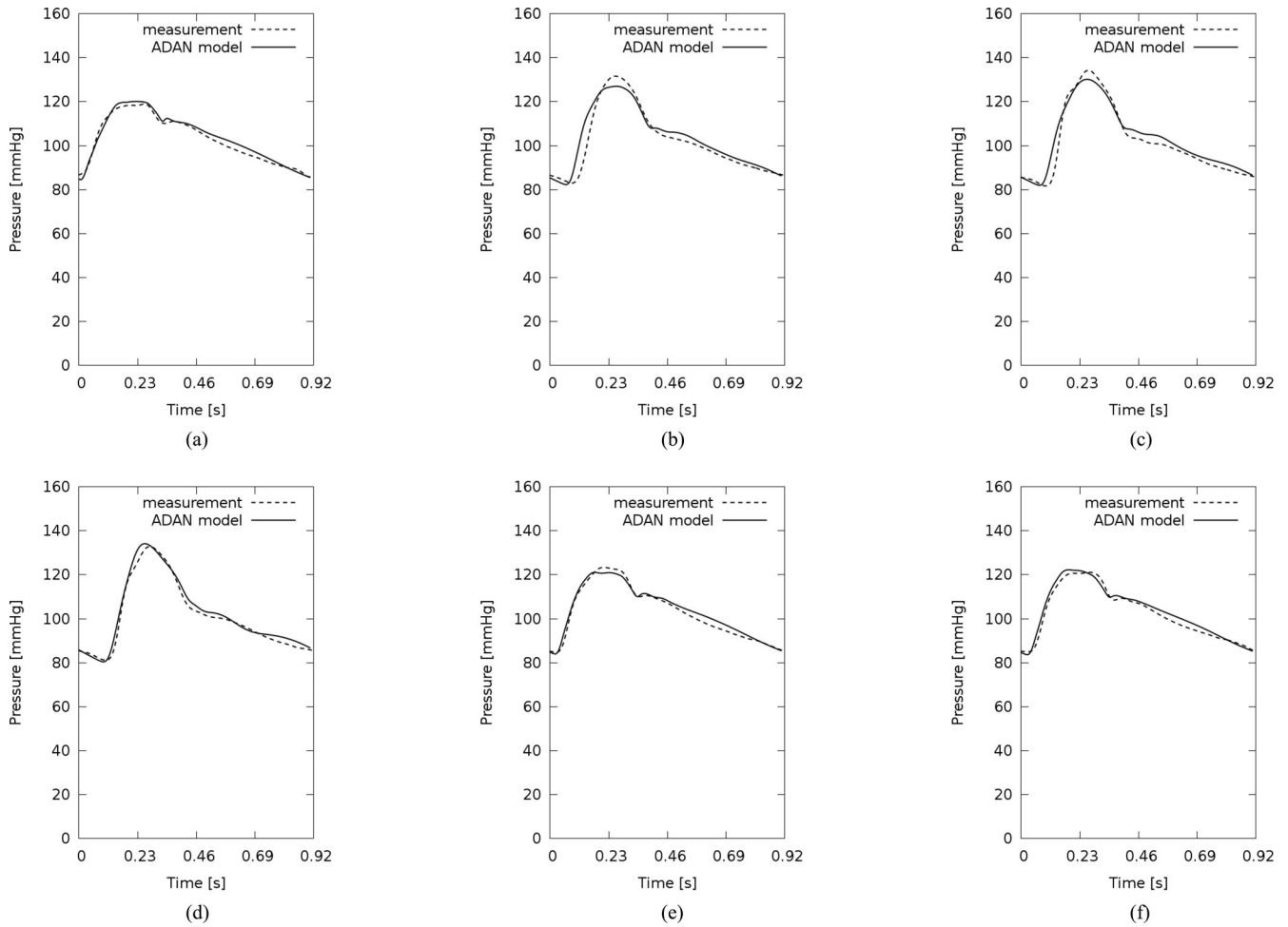


Fig. 7. Comparison of pressure waveforms predicted by the model and patient-specific measurements at different central arteries (a) Ascending aorta (b) Abdominal aorta (renals) (c) Abdominal aorta (iliac) (d) External iliac (e) Brachiocephalic trunk (f) Common carotid.

using the same criteria as for the ADAN model. Consequently, arterial lengths are the same of the ADAN model. As outflow condition, the average flow was measured in the arteries of the ADAN model corresponding to the terminal arteries of the ADAN-55 model, and terminal resistances were calculated such that this flow distribution is satisfied. Thus, in the ADAN-55 model, the total outflow is evidently a fraction of the total blood flow (77.2% of the ADAN total inflow). To make results comparable, the remaining flow (22.8%) was considered to go to the peripheral beds in the arms and legs within the ADAN-55 model, with a fraction proportional to the flow these vascular regions receive. Finally, the resistances were scaled to have the same average pressure at the aortic root.

For the terminal compliance, all Windkessel terminals of the ADAN-55 model have a compliance such that the total compliance of the model is the same (computed using the linear contribution of the elastin). Regional compliance is determined proportionally to the flow. Although a more refined compliance distribution could have been taken from the downstream vasculature in the ADAN, the present choice is taken because is a standard hypothesis assumed in the field [29], [66].

B. Healthy Condition

In the healthy condition, both models render comparable behavior in the aorta artery as shown in Fig. 8(a)–8(d). While the pressure contour is remarkable similar, the flow rate is similar during systole, and differences arise during diastole caused by the combination of reflections arriving from the periphery. At brachial and radial arteries (see Fig. 8(e)–8(f), respectively), the blood flow is considerably overestimated by the ADAN-55 model. In such cases, the ADAN model predicts a realistic average blood flow because of the existence of vascular territories along the pathway. As a consequence, the pressure drops more in the ADAN-55 model as we move toward the periphery. In the lower limb [see Fig. 8(g)–(h)], the pressure contour is similar, and the flow features differences, which can be explained by the same arguments given above for the upper limb. Waveforms at the common carotid and internal carotid arteries are also compared in Fig. 8(i)–(j), respectively. It can be seen that the predicted pressure pulse, mostly during systole, differs as we move toward the brain, caused by the existence of more arterial vessels and connections. It can be appreciated that the ADAN-55 model overestimates the flow rate pulsatility,

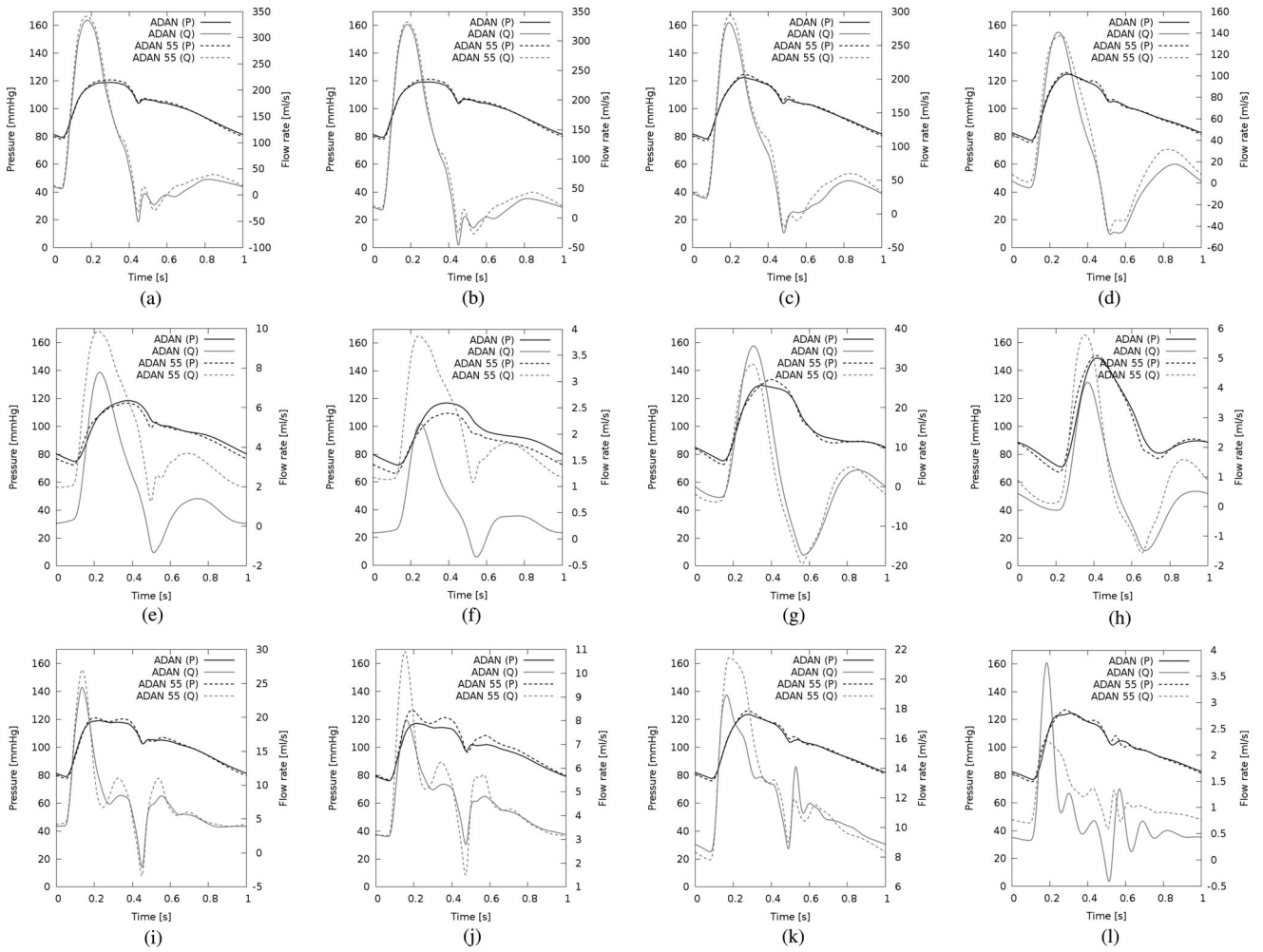


Fig. 8. Pressure (black) and flow rate (gray) waveform comparisons between ADAN model (solid line) and ADAN-55 model (dashed line) in the healthy condition at several arterial vessels (a) Aortic arch (distal) (b) Thoracic aorta (proximal) (c) Thoracic aorta (distal) (d) Abdominal aorta (infra-mesenteric) (e) Brachial (f) Radial (g) Femoral (proximal) (h) Posterior tibial (i) Common carotid (j) Internal carotid (k) Renal (l) Inferior mesenteric.

more significantly at the ICA (see normal values in Table III). Finally, waveforms at the renal artery and at the inferior mesenteric artery are compared (see Fig. 8(k)–(l), respectively). As in the previous comparisons, the pressure predicted by both models is in agreement except for subtle differences around the diastolic notch [see particularly Fig. 8(e), (j), and (l)]. As for the flow rate contour, the differences are important at both vessels (renal and inferior mesenteric). In the case of the renal artery, this could be explained by the effect of downstream vasculature and configuration of arterial walls in peripheral vessels of the ADAN model, which differs from the simple terminal model employed in the ADAN-55 model. In turn, at the inferior mesenteric artery, in addition to the previous explanation is the fact that inferior and superior mesenteric arteries are anastomosed (through the marginal artery of the colon) and the blood supply to the mesentery is accomplished by a highly intricate vascular network. This connection established a more complex hemodynamic interactions, which leads to the substantial differences observed in Fig. 8(l).

A quantitative comparison of the results is given in Table VI using the RMSE index [35]. The RMSE for the pressure is

TABLE VI
QUANTITATIVE COMPARISON OF PREDICTIONS GIVEN BY THE ADAN AND ADAN-55 MODELS

Artery	RMSE (%)	
	Flow rate	Pressure
Aortic arch	3.29	2.75
Thoracic aorta p.	3.38	2.78
Thoracic aorta d.	4.01	2.52
Abdominal aorta	8.27	2.50
Brachial	32.26	6.34
Radial	67.88	14.45
Femoral p.	9.17	4.15
Posterior tibial	21.44	6.18
Common carotid	5.59	3.38
Internal carotid	10.98	10.66
Renal	8.10	2.70
Inferior mesenteric	16.12	4.04
Vertebral	4.49	3.03

RMSE for pressure waveforms is normalized by the pulse pressure amplitude and for the flow waveforms is normalized by the systolic flow rate, p.: proximal location, d.: distal location.

TABLE VII
ALTERATION OF BLOOD FLOW IN THE PRESENCE OF A STENOSIS AT THE ICA

Artery	Variation of flow rate (%)	
	ADAN	ADAN-55
ICA l. p.	-75.28	-36.04
ICA r. p.	39.06	1.51
VA l. p.	25.63	1.61
VA r. p.	23.78	1.60
ECA l. p.	2.84	1.98
ECA r. p.	0.44	1.53
Total CBF*	-1.50	-12.96

Variations are measured relative to the average flow in the corresponding vessel at baseline condition. ICA: internal carotid artery, ECA: external carotid artery, VA: vertebral artery, CBF: cerebral blood flow, l.: left, r.: right, p.: proximal.
*: computed as the sum of distal flow at both ICAs and both VAs.

normalized by the pulse pressure amplitude, and for the flow rate it is normalized by the systolic flow. Both reference values are taken at the corresponding vessel as given by the ADAN model. The reported values support the discussion of the previous paragraph. In addition, the RMSE for the vertebral artery (VA) is presented, which will serve for reference for the next section.

From the results presented in this section, we can conclude that, with proper parameter manipulation, the results predicted by the ADAN model and by the ADAN-55 model could have a better agreement. In next sections, we provide illustrative examples of disease, which serve as solid rationale for the development of the present ADAN model.

C. Stenosis in the ICA

In this example, we introduce a resistive model in the left ICA calibrated such that the pressure drop in the ADAN model is approximately 15 mmHg. This corresponds to a stenosis with degree of constriction over 60% of the luminal diameter, as reported in [67]. Then, the same resistive model was introduced in the ADAN-55 model. Table VII presents the modification of average blood flow from the baseline condition as predicted by the ADAN model and by the ADAN-55 model. It is observed that the neck vasculature suffers significant alteration of the blood supply in the ADAN model, as compared with the ADAN-55 model. That is, the highly collateralized network supplying the brain is functional to the stenosis at the ICA, resulting in a total cerebral blood flow reduction predicted by the ADAN model of only 1.5% when compared with the exaggerated flow reduction of 12.96% given by the ADAN-55 model.

In Fig. 9, we compare hemodynamic variables in the left ICA at a postobstructive location and at the left VA. Clearly, the flow waveform is absolutely different at the ICA. The ADAN model predicts a dampened postobstructive flow waveform (almost the absence of flow pulse), differently from the ADAN-55 model that displays a resistive flow signature. The drop pressure between the healthy condition and the stenosis condition in the ADAN model is 15 mmHg, while, in the ADAN-55 model, it is overestimated, being 37 mmHg. This is the result of the ex-

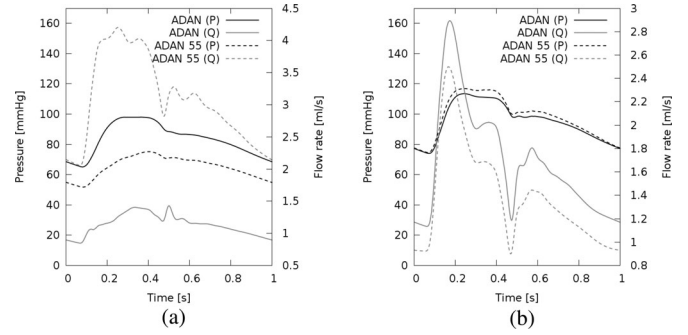


Fig. 9. Waveform comparisons between ADAN model (solid line) and ADAN-55 model (dashed line) in the presence of a stenosis in the ICA. Pressure (black) and flow rate (gray) are shown at the ICA (postobstructive) and at the VA (a) Internal carotid (b) Vertebral.

TABLE VIII
QUANTITATIVE COMPARISON OF PREDICTIONS GIVEN BY THE ADAN AND ADAN-55 MODELS

Artery	RMSE (%)	
	Flow rate	Pressure
ICA l.	142.24	57.63
ICA r.	16.57	18.34
VA l.	10.43	7.55
VA r.	9.44	7.43

RMSE for pressure waveforms is normalized by the pulse pressure amplitude and for the flow waveforms is normalized by the systolic flow rate. ICA: internal carotid artery, VA: vertebral artery, l.: left, r.: right.

istence of connectivity among vessels in the ADAN model that provides collateral pathways for the blood to reach the brain. In Table VIII, the normalized RMSE is presented for pressure and flow rate the ICA and the VA. It can be seen that these values increased with respect to the values reported in the healthy condition (see Table VI) implying that the response of two models differ more in the case of disease.

As well, we analyze the collateral function by studying the sensitivity of the blood flow to the presence of the stenosis as given by the ADAN model. This is not possible in the ADAN-55 model for obvious reasons. Fig. 10 presents the pressure and the flow rate at the ICA and at the VA, as well as the modification of the hemodynamic environment at the middle cerebral artery (MCA), the anterior cerebral artery (ACA), the posterior cerebral artery (PCA) and posterior communicating artery (PcomA). It can be seen that the right ICA [see Fig. 10(b)] and both VA [see Fig. 10(c) and (d)] conduct more blood to the brain to compensate for the flow reduction caused by the stenosis through the left ICA (see Fig. 10(a) and Table VII). This excess of blood is then sent through the anterior communicating artery (not shown in that figure) and the left PcomA, inverting the main direction of flow [see Fig. 10(k)], to feed the left ACA [see Fig. 10(e)] and left MCA [see Fig. 10(g)]. From the results, it is also noticed that the right cerebral hemisphere suffers less the consequences of the stenosis than the left hemisphere [compare Fig. 10(e)–10(f) and Fig. 10(g)–(h)],

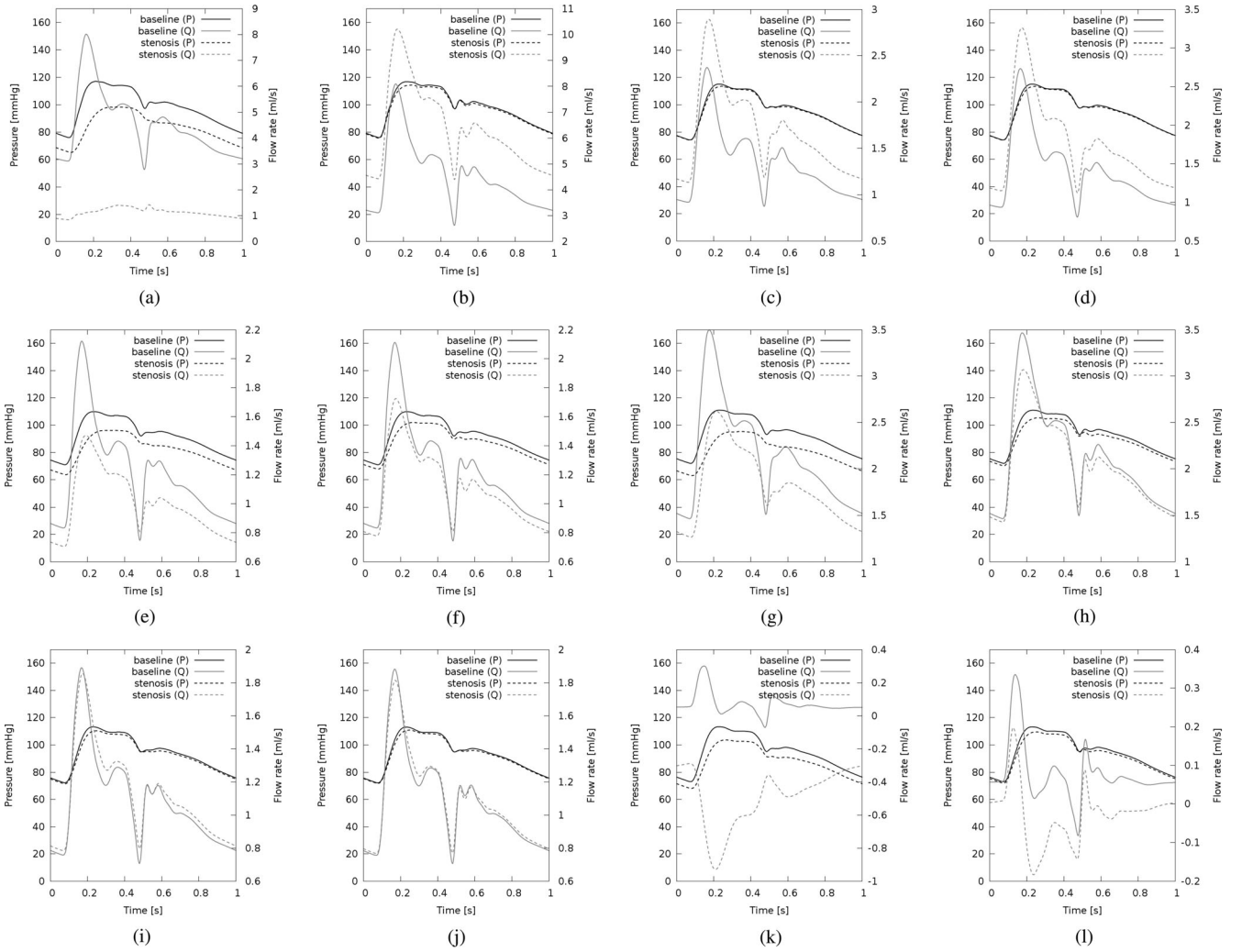


Fig. 10. Collateral function as predicted by the ADAN model in the presence of a stenosis at the ICA. Pressure (black) and flow rate (gray) waveform in the healthy (solid line) and in the case of stenosis (dashed line) (a) Internal carotid left (b) Internal carotid right (c) Vertebral left (d) Vertebral right (e) Anterior cerebral left (f) Anterior cerebral right (g) Middle cerebral left (h) Middle cerebral right (i) Posterior cerebral left (j) Posterior cerebral right (k) Posterior communicating left (l) Posterior communicating right.

while the posterior cerebral circulation is almost unaffected [see Fig. 10(i)–(j)].

Clearly, the present model is a powerful tool able to provide fundamental mechanistic insight about the regional effect of stenoses in the cerebral circulation, and its impact on associated diseases such as stroke and transient brain ischemia.

D. Stenosis in the SA

The existence of a severe stenosis in the SA proximal to the VA is known to produce the so-called subclavian steal syndrome (SSS) through which the arm “steals” blood from the brain causing vertebrobasilar insufficiency. This phenomenon is actually due to the connection between the distal SA and the ICA through the circle of Willis and the VA. In patients with this kind of disease, retrograde VA blood flow is observed and brain ischemia can be produced in the case of arm exercise.

Thus, to simulate this condition, and in the same spirit of the previous section, we consider a resistive model in the left SA proximal to the VA, which is tuned to deliver a pressure drop

in the ADAN model of approximately 10 mmHg (actually, SSS is suspected when the pressure difference between arms is over 20 mmHg). The same stenosis model is employed in the ADAN-55 model. The pathological condition is then characterized by a pressure difference between arms of 9.5 mmHg in the ADAN model and 9.9 mmHg in the ADAN-55 model.

The normalized values of the RMSE for flow rate and pressure, comparing the responses of the ADAN and ADAN-55 models, at the left VA are RMSE = 101.51% and RMSE = 18.85%, respectively. These values are larger than those reported in the healthy case (see Table VI). Particularly, the much larger value of the RMSE in the flow waveform can be explained by the retrograde blood flow predicted by the ADAN model, opposed to the unrealistic antegrade flow given by the ADAN-55 model. In Fig. 11(a), the healthy and stenosis conditions as predicted by the ADAN model are compared. In such figure, the “steal” phenomenon during systole is effectively predicted. In addition, the normalized RMSE for flow rate and pressure, comparing ADAN and ADAN-55 models, at the right VA are RMSE = 24.78%

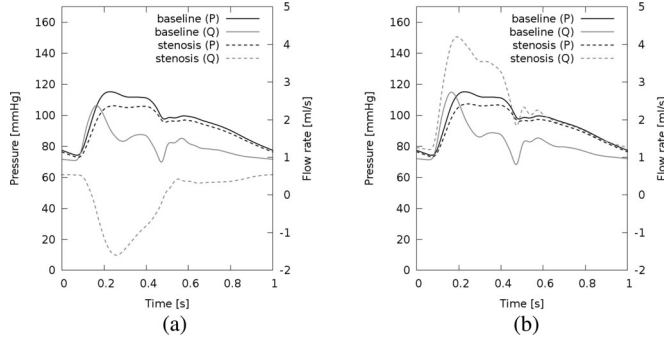


Fig. 11. Pressure (black) and flow rate (gray) waveform comparisons at the VA arteries between baseline (solid line) and SA stenosis (dashed line) conditions as predicted by the ADAN model (a) Vertebral (left) (b) Vertebral (right).

TABLE IX
ALTERATION OF BLOOD FLOW IN BRAIN VESSELS DURING SSS

Artery	Variation of flow rate (%)	
	ADAN	ADAN-55
ICA l. p.	4.48	0.55
ICA r. p.	4.53	0.56
VA l. p.	-105.46	-10.13
VA r. p.	65.62	0.57
ACA l.	1.77	—
ACA r.	1.76	—
MCA l.	0.36	—
MCA r.	0.37	—
PCA l.	-5.53	—
PCA r.	-5.50	—

Variations are measured relative to the average flow in the corresponding vessel at baseline condition. ICA: internal carotid artery, VA: vertebral artery, ACA: anterior cerebral artery, MCA: middle cerebral artery, PCA: posterior cerebral artery, l.: left, r.: right, p.: proximal, —: not present.

and $RMSE = 15.05\%$, respectively. These values reflect the difference in both models due to the increase in the blood flow given by the ADAN model, contrary to the almost invariant flow given by the ADAN-55 model. In Fig. 11(b), the flow increase with respect to the healthy condition is observed at the right VA in the case of stenosis.

The previous discussion is complemented with the results of the ADAN model summarized in Table IX about the change in the average blood flow (relative to the baseline condition) provoked by the SSS in the main cerebral arteries. As in the previous section, in the ADAN model the arteries converging to the circle of Willis modify its function, increasing the blood they conduct to compensate the insufficiency of the left VA, and ultimately to provide blood to the left arm. From the results, one sees that the major changes are in both vertebral arteries, but also the both ICAs help to supply blood to the arm. Moreover, the present model is capable of providing further insight in assessing the impact of the SSS in the brain circulation. From the table, we conclude that the anterior and middle cerebral arteries are minimally affected by the stenoses in terms of average blood flow, while the average blood flow is reduced around 10% in the posterior circulation.

VIII. VALIDITY AND LIMITATIONS

This section is devoted to describe limitations in the modeling approach, which could explain discrepancies between model predictions and observations. The following sections extend the discussion presented at the end of Section VI-C.

A. On the Description of the Cardiovascular System

The present model accounts for the description of the arterial network with an unprecedented level of morphological detail. A natural limitation in the descriptive capabilities of the present model is the lack of systemic coupling with other active elements in the cardiovascular system. Closed-loop models of the circulation incorporating cardiac mechanics are known to be relevant in shaping the pressure contour as well as in certain pathological conditions [66], [68]–[71]. Another example is the local compensation produced by the brain in the presence of stenoses [72], something that was not considered in this study. Improvement of the model depends on the kind of problem to be addressed. However, in any case, the ADAN model represents a baseline model to explore complex interactions with other subsystems, such as the venous system, the cardiac function, cerebro-spinal fluid system, central nervous system, etc.

B. On the Mathematical Modeling

Even accepting the validity of fluid mechanics equations in extremely tiny vessels, the question that remains open is about the modeling of viscous losses in such vessels. The present model employs a standard Poiseuille hypothesis for the flow. However, flow heterogeneity as well as the so-called Fahraeus and Fahraeus–Lindqvist effects can definitely pose challenges to develop an accurate model of effective viscosity at places (arterioles), where blood should be acknowledged as a suspension instead of a homogeneous fluid [73]. For example, it is widely acknowledged the shear-thinning effect caused by red blood cell aggregation. This point deserves further study when addressing in more detail problems related to microcirculation using 1-D models.

In addition, mathematical modeling using 1-D equations is limiting when trying to characterize more refined fluid dynamic factors, such as wall shear stress and pressure drop in geometrical singularities. Improved features can be found in [34] where a Womersley solution is employed to increase the description of the velocity profile and improve computation of viscous losses. As well, these aspects can be improved by resorting to enriched 1-D models [74], or by using dimensionally heterogeneous (3-D–1-D) models to simulate with high degree of detail the hemodynamics in a specific arterial district [75], [76].

C. On the Parameter Calibration

As in most works in the field, parameter calibration is a delicate point. The criteria employed to determine blood flow distribution is based on physiological and anatomical concepts [41]. In turn, calibration of arterial wall parameters constitutes the major uncertainty in the system. The large number of parameters in

the present model makes mandatory the search for morphologic laws to characterize parameters according to, for example, the size of the vessels and the amount of blood they carry. This point is starting to be addressed in the literature through the introduction of data assimilation strategies [37], [77], but further research and validation techniques are necessary.

IX. CONCLUSION

In this study, a novel model of the arterial network featuring high level of detail in the realization of the anatomical topology has been presented. This model, provided with stringent anatomical and physiological criteria for the calibration of parameters, proved to deliver predictions in agreement with data published in the specialized literature. Such predictions are not only in terms of local flow and pressure waveforms, but also in terms of global features such as network impedance, and well-known cardiovascular indexes used for predicting cardiovascular diseases. Although there is still room for a refinement of the calibration process as well as for a more comprehensive validation procedure, the presented results indicate that the basic underlying criteria to calibrate the model parameters are satisfactory. The sensitivity analysis study performed following a regional perturbation strategy has been useful to elucidate the differential impact of model parameters in the conformation of the waveforms in both central and peripheral arteries. Furthermore, the agreement between model predictions and patient-specific pressure measurements reported in this study are extremely promising. In fact, even in such adverse scenario in terms of available data, such comparisons provide strong evidences about the feasibility of targeting the ADAN model to specific cardiovascular conditions.

The novel feature of the ADAN model is the extremely detailed anatomical description of the arterial network, characterizing the model as a comprehensive simulation framework that allows to tackle, from a numerical simulation perspective, complex problems in cardiovascular research that remain poorly understood. The ADAN model presents potential impact on the study and characterization of cardiovascular diseases, organ functioning, tissue microcirculatory perfusion, pharmacokinetics, pharmacodynamics and surgical planning, just to mention some big areas of application (see Supplementary Material).

Moreover, from the modeling standpoint, in view of the intrinsic 3-D description of arterial vessels, the ADAN model turns out to be the geometrical substrate on top of which more accurate blood flow models can be set up, going to hierarchical-enriched 1-D- realizations, to 3-D-1-D multiscale approaches or even full 3-D modeling (provided available computational resources grow accordingly). We strongly believe that this model is an innovative step toward a new generation of high definition computational models to assist cutting-edge cardiovascular research.

REFERENCES

- [1] R. Nerem and J. Cornhill, "The role of fluid mechanics in atherogenesis," *J. Biomech. Eng.*, vol. 102, pp. 181–189, 1980.
- [2] M. Friedman *et al.*, "Arterial geometry affects hemodynamics. A potential risk factor for atherosclerosis," *Atherosclerosis*, vol. 46, pp. 225–231, 1983.
- [3] C. Zarins *et al.*, "Carotid bifurcation atherosclerosis. Quantitative correlation of plaque localization with flow velocity profiles and wall shear stress," *Circ. Res.*, vol. 53, pp. 502–514, 1983.
- [4] D. Ku *et al.*, "Pulsatile flow and atherosclerosis in the human carotid bifurcation. Positive correlation between plaque location and low oscillating shear stress," *Arteriosclerosis*, vol. 5, pp. 293–302, 1985.
- [5] C. Zarins *et al.*, "Shear stress regulation of artery lumen diameter in experimental atherogenesis," *J. Vasc. Surg.*, vol. 5, pp. 413–420, 1987.
- [6] M. Friedman, "A biologically plausible model of thinking of arterial intima under shear," *Arteriosclerosis*, vol. 9, pp. 511–522, 1989.
- [7] E. Gao *et al.*, "A theoretical model of cerebral hemodynamics: application to the study of arteriovenous malformations," *J. Cerebral Blood Flow Metabolism*, vol. 17, pp. 905–918, 1997.
- [8] F. Migliavacca *et al.*, "Multiscale modelling in biofluidynamics: Application to reconstructive paediatric cardiac surgery," *J. Biomech.*, vol. 39, pp. 1010–1020, 2006.
- [9] G. Pennati *et al.*, "Boundary conditions of patient-specific fluid dynamics modelling of cavopulmonary connections: Possible adaptation of pulmonary resistances results in a critical issue for a virtual surgical planning," *Interface Focus*, vol. 1, pp. 297–307, 2011.
- [10] J. Revie, D. Stevenson *et al.*, "Clinical detection and monitoring of acute pulmonary embolism: Proof of concept of a computer-based method," *Ann. Intensive Care*, vol. 1, pp. 1–33, 2011.
- [11] C. Taylor *et al.*, "Computational fluid dynamics applied to cardiac computed tomography for noninvasive quantification of fractional flow reserve. Scientific basis," *J. Amer. Coll. Cardiol.*, vol. 61, pp. 2233–2241, 2013.
- [12] C. Zarins *et al.*, "Computed fractional flow reserve (FFTC) derived from coronary CT angiography," *J. Cardiovasc. Trans. Res.*, vol. 6, pp. 708–714, 2013.
- [13] P. Hunter and P. Nielsen, "A strategy for integrative computational physiology," *Physiology*, vol. 20, pp. 316–325, 2005.
- [14] J. Ricotta *et al.*, "Cardiovascular disease management: The need for better diagnostics," *Med. Biol. Eng. Comput.*, vol. 46, pp. 1059–1068, 2008.
- [15] A. Barnard *et al.*, "Peaking of the pressure pulse in fluid-filled tubes of spatially varying compliance," *Biophys. J.*, vol. 6, pp. 735–746, 1966.
- [16] —, "A theory of fluid flow in compliant tubes," *Biophys. J.*, vol. 6, pp. 717–724, 1966.
- [17] T. Hughes and J. Lubliner, "On the one-dimensional theory of blood flow in the larger vessels," *Math. Biosci.*, vol. 18, pp. 161–170, 1973.
- [18] J. Lambert, "Fluid flow in a nonrigid tube," Ph.D. dissertation, Purdue University, West Lafayette, IN, USA, Aug. 1956.
- [19] Y. Kivity, and R. Collins, "Nonlinear wave propagation in viscoelastic tubes: application to aortic rupture," *J. Biomech.*, vol. 7, pp. 67–76, 1974.
- [20] M. Anliker *et al.*, "Nonlinear analysis of flow pulses and shock waves in arteries. Part I: Derivation and properties of mathematical model," *J. Appl. Math. Phys.*, vol. 22, pp. 217–246, 1971.
- [21] —, "Nonlinear analysis of flow pulses and shock waves in arteries. Part II: Parametric study related to clinical problems," *J. Appl. Math. Phys.*, vol. 22, pp. 563–581, 1971.
- [22] A. Noordergraaf *et al.*, "The use of an analog computer in a circulation model," *Prog. Cardiovasc. Dis.*, vol. 5, pp. 419–439, 1963.
- [23] B. Schaaf and P. Abbrecht, "Digital computer simulation of human systemic arterial pulse wave transmission: A nonlinear model," *J. Biomech.*, vol. 5, pp. 345–364, 1972.
- [24] M. Spencer and A. Deninson, "The square-wave electro-magnetic flowmeter. Theory of operation and design of magnetic probes for clinical and experimental applications," *IRE Trans. Med. Electron.*, vol. ME-6, no. 4, pp. 220–228, Dec. 1959.
- [25] N. Westerhof *et al.*, "Analog studies of the human systemic arterial tree," *J. Biomech.*, vol. 2, pp. 121–143, 1969.
- [26] A. Avolio, "Multi-branched model of the human arterial system," *Med. Biol. Eng. Comput.*, vol. 18, pp. 709–718, 1980.
- [27] J. Stettler *et al.*, "Theoretical analysis of arterial hemodynamics including the influence of bifurcations. Part I: Mathematical model and prediction of normal pulse patterns," *Ann. Biomed. Eng.*, vol. 9, pp. 145–164, 1981.
- [28] J. Stettler *et al.*, "Theoretical analysis of arterial hemodynamics including the influence of bifurcations. Part II: Critical evaluation of theoretical model and comparison with noninvasive measurements of flow patterns in normal and pathological cases," *Ann. Biomed. Eng.*, vol. 9, pp. 165–175, 1981.

- [29] N. Stergiopoulos *et al.*, "Computer simulation of arterial flow with applications to arterial and aortic stenoses," *J. Biomech.*, vol. 25, pp. 1477–1488, 1992.
- [30] S. Sherwin *et al.*, "One-dimensional modelling of a vascular network in space-time variables," *J. Eng. Math.*, vol. 47, pp. 217–250, 2003.
- [31] J. Alastruey *et al.*, "Pulse wave propagation in a model human arterial network: Assessment of 1-D visco-elastic simulations against in vitro measurements," *J. Biomech.*, vol. 44, pp. 2250–2258, 2011.
- [32] K. Matthys *et al.*, "Pulse wave propagation in a model human arterial network: Assessment of 1-D numerical simulations against in vitro measurements," *J. Biomech.*, vol. 40, pp. 3476–3486, 2007.
- [33] M. Olufsen *et al.*, "Numerical simulation and experimental validation of blood flow in arteries with structured-tree outflow conditions," *Ann. Biomed. Eng.*, vol. 28, pp. 1281–1299, 2000.
- [34] P. Reymond *et al.*, "Validation of a one-dimensional model of the systemic arterial tree," *Amer. J. Physiol. Heart Circ. Physiol.*, vol. 297, pp. H208–H222, 2009.
- [35] P. Reymond *et al.*, "Validation of a patient-specific one-dimensional model of the systemic arterial tree," *Amer. J. Physiol. Heart Circ. Physiol.*, vol. 301, pp. H1173–H1182, 2011.
- [36] N. Xiao *et al.*, "A systematic comparison between 1-D and 3-D hemodynamics in compliant arterial models," *Int. J. Num. Meth. Biomed. Eng.*, vol. 30, pp. 204–231, 2014.
- [37] D. Lombardi, "Inverse problems in 1D hemodynamics on systemic networks: A sequential approach," *Int. J. Num. Meth. Biomed. Eng.*, vol. 30, pp. 160–179, 2014.
- [38] F. Liang *et al.*, "Patient-specific assessment of cardiovascular function by combination of clinical data and computational model with applications to patients undergoing Fontan operation," *Int. J. Num. Meth. Biomed. Eng.*, vol. 30, pp. 1000–1018, 2014.
- [39] W. Dauber, *Pocket Atlas of Human Anatomy by Feneis*, 5th ed. New York, NY, USA: Thieme, 2007.
- [40] F. Netter, *Atlas of Human Anatomy*, 5th ed. New York, NY, USA: Elsevier, 2011.
- [41] P. Blanco *et al.*, "Blood flow distribution in an anatomically detailed arterial network model: Criteria and algorithms," *Biomechanics Modeling Mechanobiol.*, vol. 13, pp. 1303–1330, 2014.
- [42] HeMoLab, *ADAN-WEB application*, 2013. [Online]. Available: <http://hemolab.lncc.br/adan-web>
- [43] A. Green and P. Naghdi, "A direct theory of viscous fluid flow in pipes I. Basic general developments," *Philos. Trans. Roy. Soc. London A, Math. Phys. Sci.*, vol. 342, pp. 525–542, 1993.
- [44] A. Green *et al.*, "A direct theory of viscous fluid flow in pipes II. Flow of incompressible viscous fluid in curved pipes," *Philos. Trans. Roy. Soc. London A, Math. Phys. Sci.*, vol. 342, pp. 543–572, 1993.
- [45] K. Parker, "An introduction to wave intensity analysis," *Med. Bio. Eng. Comput.*, vol. 47, pp. 175–188, 2009.
- [46] K. Parker and C. Jones, "Forward and backward running waves in the arteries: analysis using the method of characteristics," *J. Biomech. Eng.*, vol. 112, pp. 322–326, 1990.
- [47] J. Murgu *et al.*, "Aortic input impedance in normal man: relationship to pressure wave forms," *Circulation*, vol. 62, pp. 105–116, 1980.
- [48] C. Vlachopoulos and M. O'Rourke, "Genesis of the normal and abnormal arterial pulse," *Curr. Probl. Cardiol.*, vol. 25, pp. 303–367, 2000.
- [49] S. Bhatt *et al.*, "Sonographic evaluation of the abdominal aorta," *Ultrasound Clinics*, vol. 2, pp. 437–453, 2007.
- [50] M. Revzin and J. Pellerito, "Ultrasound assessment of the mesenteric arteries," *Ultrasound Clinics*, vol. 2, pp. 477–492, 2007.
- [51] M. Wood *et al.*, "Spectral doppler signature waveforms in ultrasonography: A review of normal and abnormal waveforms," *Ultrasound Quarterly*, vol. 26, pp. 83–99, 2010.
- [52] A. Bollinger *et al.*, "Measurement of foot artery blood pressure by micromanometry in normal subjects and in patients with arterial occlusive disease," *Circulation*, vol. 53, pp. 506–512, 1976.
- [53] D. Holdsworth *et al.*, "Characterization of common carotid artery blood-flow waveforms in normal human subjects," *Physiological Meas.*, vol. 20, pp. 219–240, 1999.
- [54] M. Zhao *et al.*, "Regional cerebral blood flow using quantitative MR angiography," *AJNR Amer. J. Neuroradiol.*, vol. 28, pp. 1470–1473, 2007.
- [55] N. Westerhof and B. Westerhof, "Wave transmission and reflection of waves. "The myth is in their use", *Artery Res.*, vol. 6, pp. 1–6, 2012.
- [56] F. Fowkes *et al.*, "Ankle brachial index combined with Framingham Risk Score to predict cardiovascular events and mortality: A meta-analysis. Ankle Brachial Index collaboration," *J. Appl. Math. Phys.*, vol. 300, pp. 197–208, 2008.
- [57] M. O'Rourke and J. Hashimoto, "Mechanical factors in arterial aging: A clinical perspective," *J. Amer. College Cardiol.*, vol. 50, pp. 1–13, 2007.
- [58] Y.-L. Liang *et al.*, "Non-invasive measurements of arterial structure and function: repeatability, interrelationships and trial sample size," *Clinical Sci.*, vol. 95, pp. 669–679, 1998.
- [59] A. Avolio *et al.*, "Role of pulse pressure amplification in arterial hypertension: experts' opinion and review of the data," *Hypertension*, vol. 54, pp. 375–383, 2009.
- [60] W.-C. Yu *et al.*, "Brachial-ankle vs carotid-femoral pulse wave velocity as a determinant of cardiovascular structure and function," *J. Human Hypertension*, vol. 22, pp. 24–31, 2008.
- [61] J. Sugawara *et al.*, "Brachial-ankle pulse wave velocity: An index of central arterial stiffness?" *J. Human Hypertension*, vol. 19, pp. 401–406, 2005.
- [62] A. Rohrer *et al.*, "Transcranial Doppler ultrasound blood flow velocity and pulsatility index as systemic indicators for Alzheimer's disease," *Alzheimer's Dementia*, vol. 7, pp. 445–455, 2011.
- [63] B. Güngör *et al.*, "Aortic stiffness is increased in patients with premature coronary artery disease: A tissue Doppler imaging study," *J. Cardiol.*, vol. 63, pp. 223–229, 2014.
- [64] G. de Simone *et al.*, "Stroke volume and cardiac output in normotensive children and adults assessment of relations with body size and impact of overweight," *Circulation*, vol. 95, pp. 1837–1843, 1997.
- [65] J. Wang and K. Parker, "Wave propagation in a model of the arterial circulation," *J. Biomech.*, vol. 37, pp. 457–470, 2004.
- [66] F. Liang and H. Liu, "A closed-loop lumped parameter computational model for human cardiovascular system," *JSME Int. J.*, vol. 48, pp. 484–493, 2005.
- [67] J. Dewese *et al.*, "Anatomic and hemodynamic correlations in carotid artery stenosis," *Stroke*, vol. 1, pp. 149–157, 1970.
- [68] F. Liang *et al.*, "Multi-scale modeling of the human cardiovascular system with applications to aortic valvular and arterial stenoses," *Med. Biol. Eng. Comput.*, vol. 47, pp. 743–755, 2009.
- [69] —, "Biomechanical characterization of ventricular-arterial coupling during aging: A multi-scale model study," *J. Biomech.*, vol. 42, pp. 692–704, 2009.
- [70] J. Mynard and P. Nithiarasu, "A 1D arterial blood flow model incorporating ventricular pressure, aortic valve and regional coronary flow using the locally conservative galerkin (LCG) method," *Commun. Numerical Methods Eng.*, vol. 24, pp. 367–417, 2008.
- [71] L. Müller and E. Toro, "A global multiscale mathematical model for the human circulation with emphasis on the venous system," *Int. J. Num. Meth. Biomed. Eng.*, vol. 30, pp. 681–725, 2014.
- [72] J. Alastruey *et al.*, "Modelling the circle of Willis to assess the effects of anatomical variations and occlusions on cerebral flows," *J. Biomech.*, vol. 40, pp. 1794–1805, 2007.
- [73] A. Popel and P. Johnson, "Microcirculation and hemorheology," *Annu. Rev. Fluid Mech.*, vol. 37, pp. 43–69, 2005.
- [74] D. Amadori *et al.*, "Derivation and analysis of a fluid-dynamical model in thin and long elastic vessels," *Netw. Heterogeneous Media*, vol. 2, pp. 99–125, 2007.
- [75] P. Blanco *et al.*, "On the potentialities of 3D–1D coupled models in hemodynamics simulations," *J. Biomech.*, vol. 42, pp. 919–930, 2009.
- [76] P. Blanco *et al.*, "Assessing the influence of heart rate in local hemodynamics through coupled 3D–1D–0D models," *Int. J. Num. Meth. Biomed. Eng.*, vol. 26, pp. 890–903, 2010.
- [77] M. Khalifé *et al.*, "Estimating absolute aortic pressure using MRI and a one-dimensional model," *J. Biomech.*, vol. 47, pp. 3390–3399, 2014.

Authors' photographs and biographies not available at the time of publication.